RSC Advances

PAPER

View Article Online
View Journal | View Issue

Cite this: *RSC Adv.*, 2025, **15**, 8385

Enhancing output efficiency in self-powered hybrid nanogenerators with micro-pyramid surface design using ceramic/polymer film for flexible wearable electronic devices

Gwangseop Lee,†[ab] Fiza Asif,†[c] Saad Ur Rahman,[c] Muhammad Zubair Khan,*[d] Adnan Maqbool,[e] Rizwan Ahmed Malik,[f] Usman Khan,[g] Osama Gohar,[h] Mohsin Ali Marwat,[i] Hafiz Muhammad Waseem Khalil,[j] Jung-Hyuk Koh*[ab] and Mohsin Saleem *[c]

Self-powered sensors are increasingly valued for their eco-friendly and energy-efficient design, making them ideal for sustainable applications. As global energy demand rises and carbon emissions increase, there is a shift toward renewable energy sources like solar and wind. Advanced sustainable energy devices, such as piezoelectric and triboelectric nanogenerators, show promises for capturing untapped energy, supporting the development of portable, green devices. While commercialization of triboelectric materials is limited, they hold strong potential for large-scale energy harvesting. This study investigates how tailored surface topography can enhance the electrical output of a hybrid nanogenerator. We developed a hybrid piezoelectric and triboelectric nanogenerator (HBNG) using a $BaTiO_3$-PDMS composite (containing 10–20 vol% barium titanate in polydimethylsiloxane). Micron-sized pyramid structures of 20% BT/PDMS were created on the film through optical lithography, while scanning electron microscopy and X-ray diffraction were used to assess the composite's crystal structure and phase characteristics. Altering the film's surface morphology led to substantial improvements in electrical performance, with voltage increasing from 28 V in the pristine film to 92 V in the micro-pyramid patterned film, and current rising from 2.7 μA to 11.0 μA. The enhanced power density and cyclic test suggests that surface topography optimization is highly effective, supporting long-term cyclic operation, and energy storage in capacitors. This work highlights the potential of surface-engineered nanogenerators in advancing sustainable, self-powered technologies.

Received 4th December 2024
Accepted 14th February 2025

DOI: 10.1039/d4ra08556f

rsc.li/rsc-advances

Introduction

In recent decades, extensive research has focused on low-power energy harvesting from environmental sources such as vibrations, light, and wind, which would otherwise be wasted. Among these sources, kinetic energy in the form of vibrations, friction, and random displacement has garnered particular attention from researchers. This energy can be harnessed to power low-power and ultra-low-power electronic devices with wireless connectivity.[1–8] To extract kinetic energy, there are various energy harvesting strategies using electromagnetic,[9] electrostatic,[10] piezoelectric,[11] triboelectric,[12] pyroelectric, and thermoelectric mechanisms. Among these, piezoelectric and triboelectric energy harvesting utilize quite efficient

[a]*Graduate School of Intelligent Energy and Industry, Chung-Ang University, Seoul, Republic of Korea. E-mail: jhkoh@cau.ac.kr*

[b]*School of Electronics and Electrical Engineering, Chung-Ang University, Seoul, South Korea*

[c]*School of Chemical and Materials Engineering (SCME), National University of Sciences and Technology (NUST), Islamabad, Pakistan. E-mail: mohsin.saleem@scme.nust.edu.pk*

[d]*Department of Materials Science & Engineering, Pak-Austria Fachhochschule: Institute of Applied Sciences and Technology, Mang, Haripur 22621, KPK, Pakistan. E-mail: zubair.khan@fcm3.paf-iast.edu.pk*

[e]*Department of Metallurgical and Materials Engineering, University of Engineering and Technology (UET), Lahore 54890, Pakistan*

[f]*Department of Mechanical Engineering, College of Engineering, Prince Sattam Bin Abdulaziz University, Al-kharj 11942, Saudi Arabia*

[g]*School of Electrical Engineering and Computer Science, National University of Sciences and Technology, Sector H-12, Islamabad, 44000, Pakistan*

[h]*Department of Mechanical and Electrical Systems Engineering, Graduate School of Engineering, Kyoto University of Advanced Science, Gotanda-cho, 18 Yamanouchi, Ukyo-ku, Kyoto, 615-8577, Japan*

[i]*Ghulam Ishaq Khan (GIK) Institute of Engineering Sciences and Technology, Topi, 23640, Pakistan*

[j]*Department of Electrical Engineering, College of Engineering and Technology, University of Sargodha, Sargodha 40100, Pakistan*

† Both authors contribute equally.

mechanisms because they are inexpensive, environmentally friendly, and have high output performance.[10,12–20]

Nanogenerators have gained significant attention in renewable energy research for their capability to harness mechanical energy from the surrounding environment. Among them, triboelectric nanogenerators (TENGs) stand out due to their straightforward design, a wide variety of material options, easy of fabrication, and cost efficiency.[21] Recently, TENGs have been employed to capture mechanical energy from various sources, including wind, blood flow, eye movements, typing actions, and ocean waves. Moreover, nanogenerators have found applications in powering a variety of sensors, such as pressure, mercury, photodetector, humidity, ion, and health monitoring sensors.[21] However, a key challenge in TENG technology is the instability in surface friction, which leads to variations in triboelectric performance over time. Frictional heat generated during the operation of TENGs is known to impair performance and longevity. To address this, shape memory materials like polyurethane utilize this heat, improving performance by altering key parameters such as the dielectric constant and charge density. Additionally, TENGs perform better in critical touch/non-touch states when approaches like ferromagnetic cilia-based TENGs (FC-TEGs) are employed, as they help sustain output without increased wear. The application of nonpolar semisolid lubricants further reduces friction and enhances the mechanical lifespan of TENGs. These innovations help mitigate the limitations of friction and wear, leading to more efficient and durable energy-harvesting devices.[22] However, it is not appropriate to fabricate by pristine materials because they exhibit low sensitivity and output power. The power density of the energy harvester using conventional materials for TENG is generally low, about 0.03–0.9 mW cm^{-2}.[23] Piezoelectric Nanogenerators (PENG) produce relatively low output power when used independently.[24] The output is in the ranges of nano-amperes and low voltages. Recent approaches in architected triboelectric and piezoelectric materials have shown significant advancements in energy harvesting and sensing applications. Nanogenerators based on piezoelectric or triboelectric materials have emerged as an attractive cost-effective technology for harvesting energy from renewable sources and for human sensing and biomedical applications.[25] The development of novel biocompatible soft materials and micro/nano-structured or chemically functionalized interfaces has opened new opportunities in this field.

One interesting approach is the hybridization of piezoelectric and triboelectric effects in coupled nanogenerators (HBNG). These devices can make full use of mechanical energies and achieve both higher output and sensing performance.[26] The integration concept and performance enhancement strategies of HBNG have been focused on structural simplification and efficiency improvement, leading to the development of all-in-one mechanical energy-scavenging and sensing devices. Hence it is quite effective to incorporate piezoelectric materials with triboelectric materials to fabricate hybrid PENG and Triboelectric Nanogenerator (TENG) devices.[26] However, Hybrid piezoelectric/triboelectric nanogenerators (HBNG) have delivered higher outputs in the ranges of nano-amperes and low voltages.

The global market revenue was estimated to be about 1B in 2020, which is anticipated to rise to € 3.2B by the end of 2027, with the contribution of nanogenerators in automobile and biomedical products reaching ~ € 59M-with an annual growth rate of more than 10%. This rapidly growing HBNG revenue in these sectors are inspiring to overcome the manufacturing barriers and material limitations and their performance in different medical sectors, which are now incorporated into millions of patients and this number is predicted to increase tenfold by 2030.[27] The main component is the TENG, and PENG is a supporting material to enhance electrical power generation. TENG is based on the phenomena of triboelectrification and electrostatic induction in which a material becomes electrically charged after it is brought into contact with a different material through friction, therefore the output performance of TENG is related to materials that are being utilized, and the surface morphology corresponding to the contact area.[28–35] Although there has been a great use of these techniques, they are very likely to become less popular as they have the disadvantage of producing very low output voltage and when scaled to a lesser size, their output performance is affected which leads to the problem of not being able to miniaturize the device. When an improved and creative structure is implemented with the usage of superior materials to increase the output, the cost of the device also goes up, which is not so effective in the long run and limits its application as a sustainable energy harvesting device. For TENG devices, neither magnets nor coils are required, they are inexpensive, have light mass, and can be fabricated using organic material as well. Furthermore, a self-powered electronic skin nanogenerator based on triboelectric and mechanoluminescent properties has been developed, capable of distinguishing multiple stimuli through a strain-sensitive mechanoluminescent layer.[36]

Due to their simplicity, wide range of materials, and cost-effective production, TENGs have become widely popular in different applications. Researchers have explored numerous materials, including polymers, metals, and composites, to enhance the triboelectric effect and thus improve the device's efficiency. Common materials include polydimethylsiloxane (PDMS),[37] polytetrafluoroethylene (PTFE),[38] and other polymers that offer a high surface charge density.

Despite change in the crystal structure of the materials, the surface morphology plays a vast role in increasing the output performance of TENG devices, increasing the surface contact area can generate more triboelectric charge during the contact and friction process. Different structures and designs have been investigated to produce high-performance TENG devices.[28–35] Initially, the scope for TENG was limited to micro-scale energy harvesting to be used for electronic network applications, but gradually their scope was extended into many useful applications including biomedical sensors, self-powered devices, actuators.[28–35] This can be done by patterning the surface with different structures at the micro-scale *i.e.*, cubes, semi-circles, and pyramids. Among the choice of materials in the triboelectric series, PDMS is an excellent candidate as it has excellent

thermal, elastic, and mechanical properties and is environmentally stable. PDMS has a significant ability to gain electrons and stands out due to its flexibility, transparency, and durability.[37,39–45] To improve the electrical, thermal, and dimensional stability of PDMS, ceramic fillers can be incorporated into it to synthesize a composite.[26] For this purpose, barium titanate (BT) is a good choice of material to be used as the ferroelectric and piezoelectric material in the hybrid nanogenerator. The pyroelectric effect in $BaTiO_3$ facilitates charge generation due to temperature variation, offering further energy harvesting potential. This phenomenon is well-suited for use in self-powered sensing and energy harvesting applications and works in conjunction with triboelectric and piezoelectric effects.[20] BT is a ferroelectric material; it has a perovskite structure, and can attain four crystal structures according to the change in temperature.[46–48] The phase diagrams of BT show that the phase transitions occur at quite low temperatures which makes them an attractive candidate for probing mechanisms of enhanced piezoelectricity.[49–52] Above the Curie temperature BT shows a cubic crystal system, but at temperatures lower than the T_c, its structure changes from cubic to tetragonal, with the orientation of dipole moment, which results in ferroelectricity in the material. The piezoelectric coefficient (d_{33}) value of BT synthesized by a solid-state reaction is almost 190 pC N^{-1} and the dielectric permittivity for BT is 1670 at ambient temperature, hence it is suitable to be used for energy harvesting purposes owing to its high dielectric permittivity, which leads to high power capabilities from $E = (1/2)CV^2$.[53–57] Several efforts have been made to better utilize the spontaneous polarization of $BaTiO_3$, including controlling the morphology of the materials, building heterojunctions, and creating small-sized devices for energy harvesting applications. Combining the above-mentioned advantages into BT-based NG is promising research and surface morphological changes make it a potential candidate for various applications.[53–57] The Hybrid Nanogenerator (HBNG) can be used to draw high electrical energy outputs. The devices can potentially be used as wearable tactile sensors and for energy harvesting. The constant motion of water, industrial vibrations, human body movement, and road vibrations can be effectively transformed into energy and used as a constant supply of electricity without any interruption.[58–61]

The present article investigates the impact of modifying the surface morphology of the BT-PDMS film to enhance its contact area. Also, we propose highly sensitive HBNG with enhanced voltage and current by using the micro pyramid pattern incorporated with BT and PDMS. The BT particles having different concentrations of PDMS were investigated and optimized. With these changes, the output voltage of the HBNG device showed a noticeable increase, accompanied by a rise in current. The HBNG fabrication technology holds a viable potential in electrical flexible devices, biomedical, sensors applications.

Experimental procedure

Materials

$BaCO_3$ (Sigma-Aldrich) and TiO_2 (Sigma-Aldrich), silicone elastomer (Sylgard 184 A purchased from Dow Corning Inc., USA), silicone elastomer curing agent (Sylgard 184 B purchased from Dow Corning Inc., USA), toluene (Sigma-Aldrich), Kapton tape, copper Tape, Copper wires, Double Sided Tape (M&G Magic Nano Tape), Al foil (Diamond Paper Aluminum).

Synthesis and sintering of $BaTiO_3$ (BT)

$BaCO_3$ and TiO_2 powders from Sigma-Aldrich were used in a solid-state reaction technique to produce $BaTiO_3$ particles. Using ethanol as a dispersion medium, the powder mixture was first ball-milled for 24 hours at 250 rpm. The slurry was milled and then dried for 24 hours at 80 °C in an oven. After drying, the powder was calcined for two hours at 850 °C with a regulated heating and cooling rate of 5 °C per minute. The calcined powder was finally dried for an additional 24 hours at 80 °C after undergoing a second ball-milling procedure in ethanol for 12 hours at 250 rpm. An agate mortar was used to grind and homogenize the powder once it had dried. The powder was compressed into pellets using cold isostatic pressing at 200 bars in preparation for sintering. These compressed pellets were then sintered for four hours at 1100 °C with a heating rate of 5 °C per minute in a muffle furnace.

Fabrication of mold

The three-dimensional micro pyramid structures were prepared by lithography on a silicon mold. The specifications of the structure are such that the base of the pyramid is 61 μm × 61 μm, the top of the pyramid is 13 μm × 13 μm and the height of the pyramid is 34 μm as shown in Fig. 3.

Fabrication of BT-PDMS film

A 10, 20 vol% BT were loaded into Polydimethylsiloxane (PDMS) such that the particles were first mixed with toluene by magnetic stirring for 30 min, and the slurry was then sonicated with an ultra-sonication bath for an hour. After sufficient mixing of BT and toluene, silicone elastomer and its curing agent were added to the solution by a ratio of 10 : 1. The solution was then left for magnetic stirring for 1 hour. The films were fabricated by solution casting methods by two different molds *i.e.*, silicon mold with micro-pyramid structures and on Kapton tape with a regular surface. Both types of samples were left in a drying oven for overnight drying at 90 °C subsequently, the films were peeled off the substrates as shown in Fig. 1.

Assembly of nanogenerator

For the fabrication of the nanogenerator, BT-PDMS composite film was used as a tribo-negative layer, Al foil served the purpose of the tribo-positive layer as well as the electrodes, and Cu wires were used to make connections. For this nanogenerator, contact separation mode was employed by using four springs on the corners and Kapton tape was used externally to hold the device and protect the films from the environment. BT were synthesized using the solid-state method and were dispersed into the PDMS elastomer matrix. The two types of films were formed, *i.e.*, one with pyramid patterns on the surface and the second

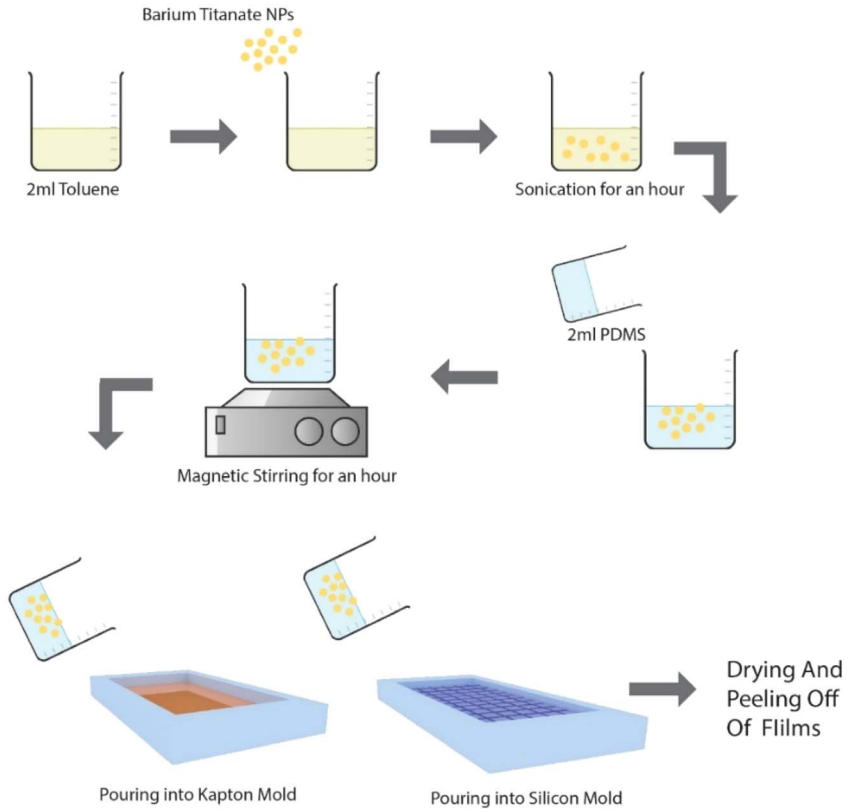

Fig. 1 Schematic representation of the fabrication steps for PDMS-BT in toluene is sonicated, mixed with PDMS, stirred, poured into molds, dried, and peeled off.

one with the different composition of regular surfaces and both films had a contact area of 4×4 cm^2.

Characterizations

Several analytical methods were used to characterize the $BaTiO_3$ (BT) samples. To determine crystalline phases, X-ray diffraction (XRD) was carried out using a Bruker 2D Phaser (2nd Gen) fitted with Cu/Kα radiation. Energy Dispersive X-ray Analysis (EDX) and a Scanning Electron Microscope (SEM) model JEOL JSM-6590A were used for morphological and compositional analysis. Using SEM imaging, structural characteristics of silicon mold patterning and BT-PDMS composite films were also investigated. Using a TA Instruments SDT Q600, thermogravimetric and differential thermal analysis (TG/DTA) was carried out in an ambient setting throughout a temperature range of 50 °C to 1050 °C at a heating rate of 10 °C min^{-1}. Vibrational modes were captured using Raman spectroscopy (NTEGRA SPECTRA, NT-MDT) throughout a wavelength range of 50 cm^{-1} to 1000 cm^{-1}. An oscilloscope (RIGOL Digital Oscilloscope DS1000E series) was used to get the output voltage and current waveforms using a mechanical force. Silver electrodes were coated on both sides of the sintered pellet in order to assess its dielectric characteristics. An impedance analyzer (Agilent tech 4294A, Malaysia) was used to quantify the dielectric constant and tangent loss between 10 kHz and 1 MHz (Fig. 2).

Results and discussions

The crystal structure of synthesized $BaTiO_3$ powder samples were characterized by an X-ray diffractometer with Cu/Kα radiation. In Fig. 3(b), the diffraction peaks for the prepared sample

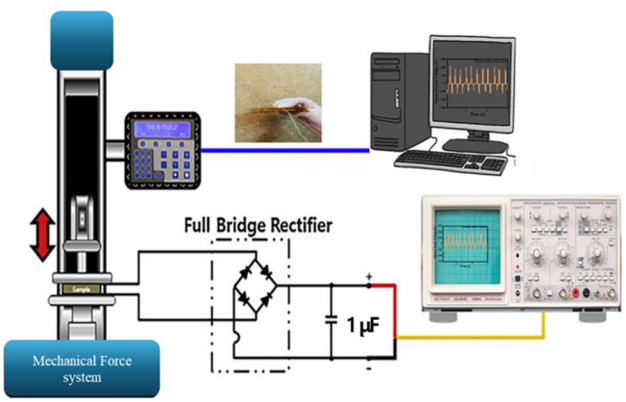

Fig. 2 Schematic of the measurement setup for the HBNG device, showing the mechanical force application system, full bridge rectifier circuit, and data acquisition setup. The system measures open-circuit voltage and short-circuit current, with a capacitor used for energy storage. The setup includes an oscilloscope and computer for real-time monitoring and analysis of the generated electrical signals under applied mechanical forces.

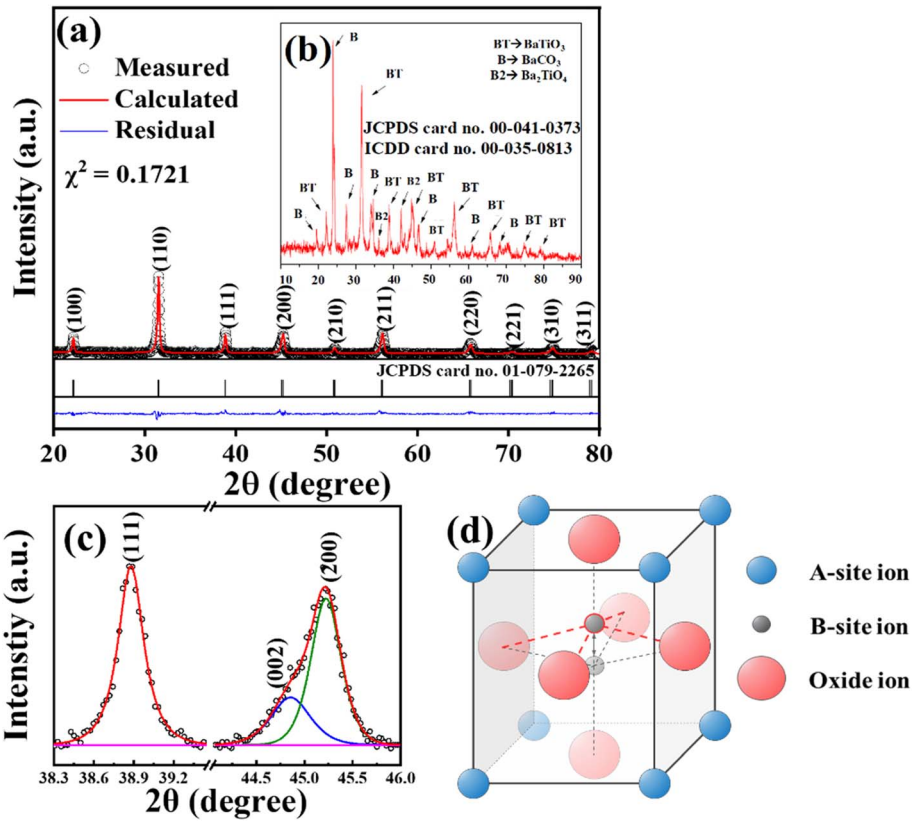

Fig. 3 (a and b) XRD patterns of barium titanate ($BaTiO_3$) powder and sintered samples at 850 °C and 1150 °C, showing phase evolution with temperature, with peaks for $BaTiO_3$ (BT), $BaCO_3$ (B), and Ba_2TiO_4 (B_2). (c) Rietveld analysis of the 1150 °C sintered sample, demonstrating precise peak fitting and quantitative phase composition, which confirms high crystallinity and structural refinement of $BaTiO_3$. (d) Crystal structure schematic of $BaTiO_3$, illustrating the perovskite lattice with Ba at the corners, Ti at the center, and O ions on the faces, a structure crucial for its ferroelectric properties.

calcined at 850 °C matched with the JCPDS card no. 01-079-2265, corresponding to tetragonal phase $BaTiO_3$ with space group *P4mm*. The observed peaks at 2θ of 22.06°, 31.57°, 38.80°, 44.85°, 50.09°, 56.26°, 65.91°, 74.91°, 79.17° correspond to the (100), (101), (111), (002), (102), (211), (202), (301), and (113) planes, respectively. There are some extra peaks belonging to $BaCO_3$ and Ba_2TiO_4 corresponding to JCPDS card no. 00-041-0373 and ICDD card no. 00-035-0813 respectively. The presence of $BaCO_3$ and Ba_2TiO_4 indicates that the reaction was insufficient at the calcination temperature, therefore by products can be removed when the material is sintered at higher temperatures. The lattice parameters of $BaTiO_3$ by Rietveld analysis of sintered sample in Fig. 3(a) are shown in Table 1. The values of *a*, *c*, and the *c*/*a* ratio exhibit index of tetragonality behavior of the $BaTiO_3$. Full-width half maximum (FWHM) and concentration of the tetragonal phase was analyzed and measured by Rietveld analysis. The crystallite size of $BaTiO_3$ was 4–7 μm. The absence of secondary peaks or impurities in the XRD pattern of the sintered $BaTiO_3$ sample at 1150 °C indicates a pure phase formation without significant side reactions. The sharp diffraction peaks of $BaTiO_3$ (JCPDS 01-079-2265) and the split (200) peak around 2θ range in 44°–45°, as illustrated in Fig. 3(c) using Rietveld analysis, confirm the presence of the tetragonal phase and demonstrate the sample's high crystallinity. The

Table 1 Summarize the lattice parameters of the $BaTiO_3$ powder by Rietveld analysis

	Centre peak		FWHM	Crystallite size (μm)	Concentrate (%)	*a*	*c*	*α*	*c*/*a*
Tetragonal	**111**					4.007	4.038	90	1.00775
	111T	38.8784	0.22509	7.913	100				
	200								
	002T	45.2234	0.36821	4.089	70.358				
	200T	44.8564	0.47837	5.346	29.642				

refined lattice parameters suggest a c/a ratio, which is a hallmark of the tetragonal phase essential for piezoelectric activity as mentioned in Table 1.

Fig. 3(a) shows the schematic illustration of the specification and layout of pyramid surface morphology engineered on the BT-PDMS (20%) surface. By increasing the contact area through these micro-pyramids in the composite film, it is expected to yield a higher electrical output due to more effective energy transfer and interaction with its uniform pyramid environment as compared to the pristine film. Scanning electron microscopy (SEM) and optical images in Fig. 4(b and c) provide a visual confirmation of the mold's micro-pyramid-structure, captured at different magnifications. These images show a detailed, magnified structure that reveal the perfect texture of the mold, leading to the uniformity of the structure, ensure the structure meets the intended design (base of the pyramid is 61 μm × 61 μm, the top of the pyramid is 13 μm × 13 μm and the height is 34 μm). The pyramids are at the intervals of 40 μm, and due to the regularity and high-density topography of the film produced by the mold. This consistency is a key factor to maintaining uniform contact across the film, which ultimately affects HBNG performance. Fig. 5(a–f) shows the SEM images of BT particles at different magnifications. The images revealed that the particles have a uniform structure and are well dispersed with a spherical morphology. The sizes of particles range from 150 nm to 270 nm. Such consistent shapes and dispersion are advantageous, to ensure the uniform distribution of BT particles in PDMS matrix, leading to the film's homogeneous structural and morphological properties. Elemental analysis and mapping of BT was performed by the EDS detector attached to the SEM. EDS analysis provide the information of elemental composition and confirmed the desired elements barium (Ba), titanium (Ti) and oxygen (O), respectively. Mapping along with Energy Dispersive X-ray spectroscopy (EDS) visualized the distribution of Ba, Ti and O in BT, verifying the uniform distribution of these elements with the BT materials to avoid agglomeration in the film as shown in Fig. 5(h).

In Fig. 6, micro pyramid pattern shows the clear and uniform distribution of micro-pyramids pattern of the BT-PDMS (20%) film structure. This regularity in patterning indicates a well-structured topography, essential for HBNG that relies on consistent surface properties. The BT-PDMS (20%) films reveal the clear integration of the BT particles in the PDMS matrix. These particles are submerged in the PDMS matrix, ensuring

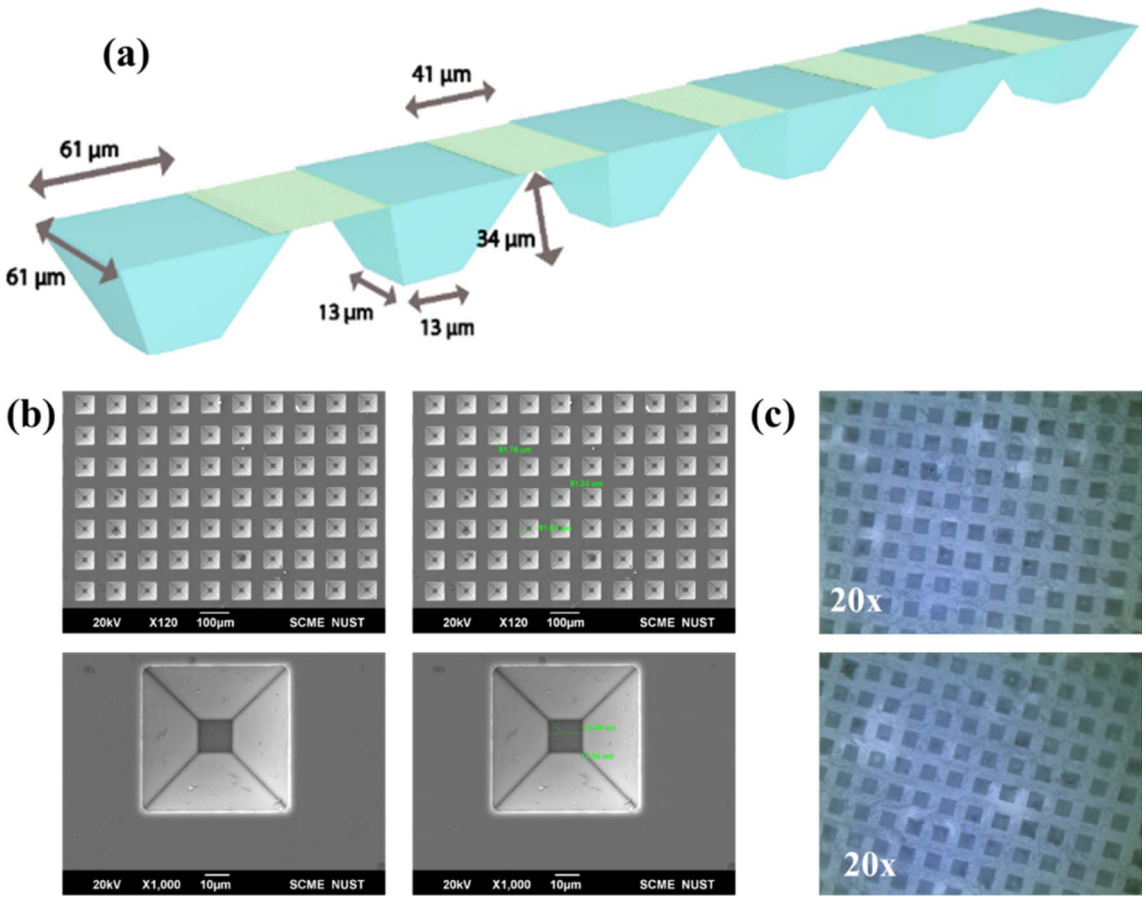

Fig. 4 (a) Schematic showing detailed specifications of the micro-pyramidal patterning with precise measurements of dimensions. (b) SEM images at various magnifications display the uniform arrangement and accuracy of the micro-pyramidal structures on the silicon mold. (c) Optical images at 20× magnification reveal the patterned surface of the silicon mold, demonstrating the consistency and clarity of the micro-structured design.

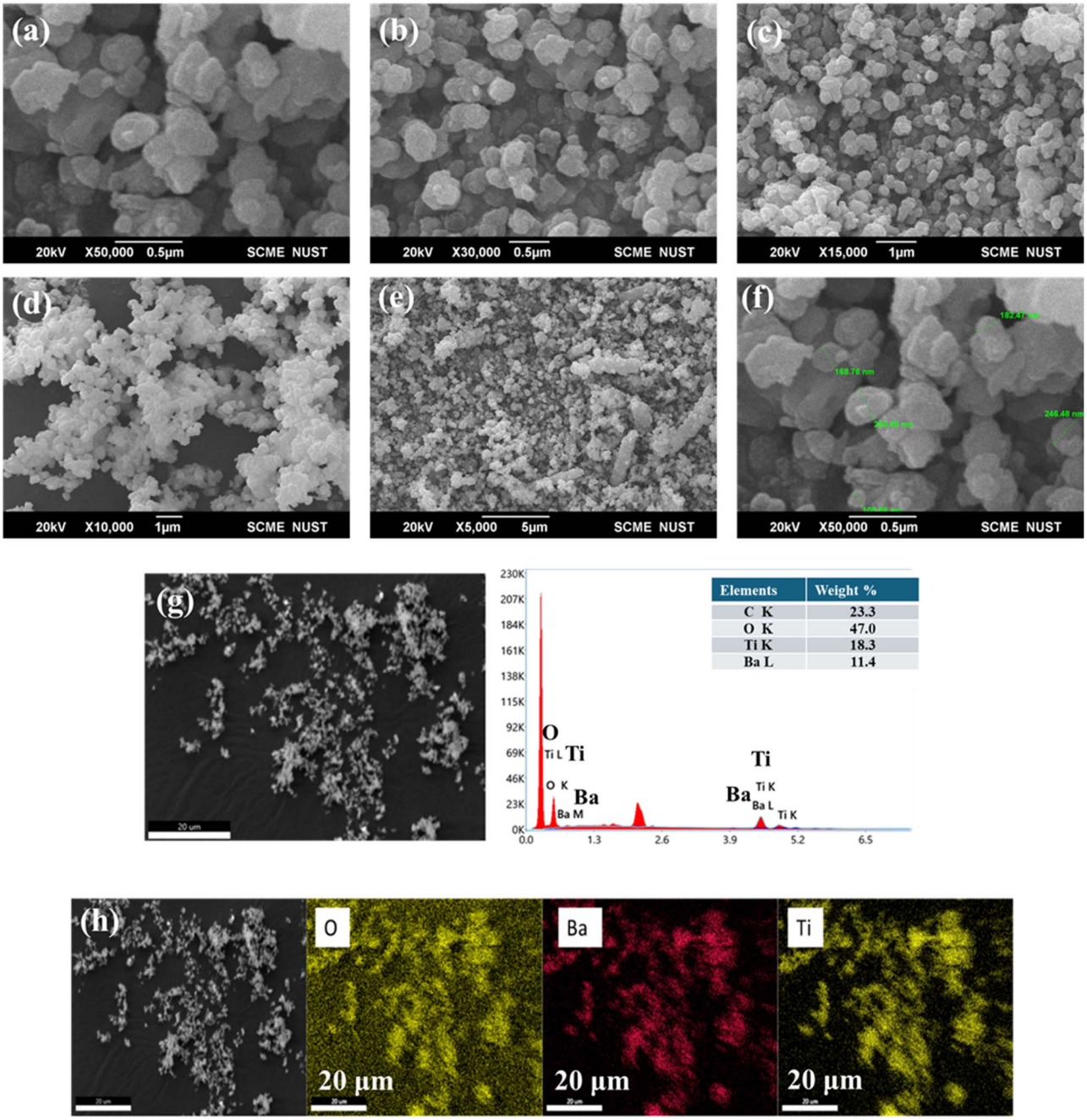

Fig. 5 (a–f) SEM images of barium titanate ($BaTiO_3$) powder at various magnifications, displaying particle morphology and size distribution. (g) EDS analysis for elemental composition, confirming the presence of Ba, Ti, O, and C in the sample. (h) Elemental mapping images for Ba, Ti, and O, showing uniform distribution of these elements within the $BaTiO_3$ powder, indicating consistent material composition.

the film's mechanical stability and functional surface area. The EDS analysis was also conducted to identify the elemental composition of BT within the PDMS film.

Thermogravimetric analysis was conducted to study the thermal stability and decomposition behavior of the synthesized BT material, tracking the weight loss of the material as a function of temperature as shown in Fig. 7(a). There are several weight loss-steps that occurred during the measurements when the temperature is increased from 25 °C to 1050 °C at a rate of 10 °C min^{-1}. Throughout this temperature span, the BT material experienced an overall weight loss of 0 to 4.5%. In the initial phase (P1), the significant first weight loss is observed sharply at 300 °C. This dramatic weight loss is likely due to the removal and burnout of residual organics arising during the synthesis of material, along with the release of moisture during high temperatures. In the second phase (P2), additional, more gradual weight loss is observed at around 800 °C, likely caused by the attributed to the amount of chemisorbed water or hydroxyl ion incorporated in the $BaTiO_3$ samples. The first phase (P1) shows pronounced weight loss than in to second

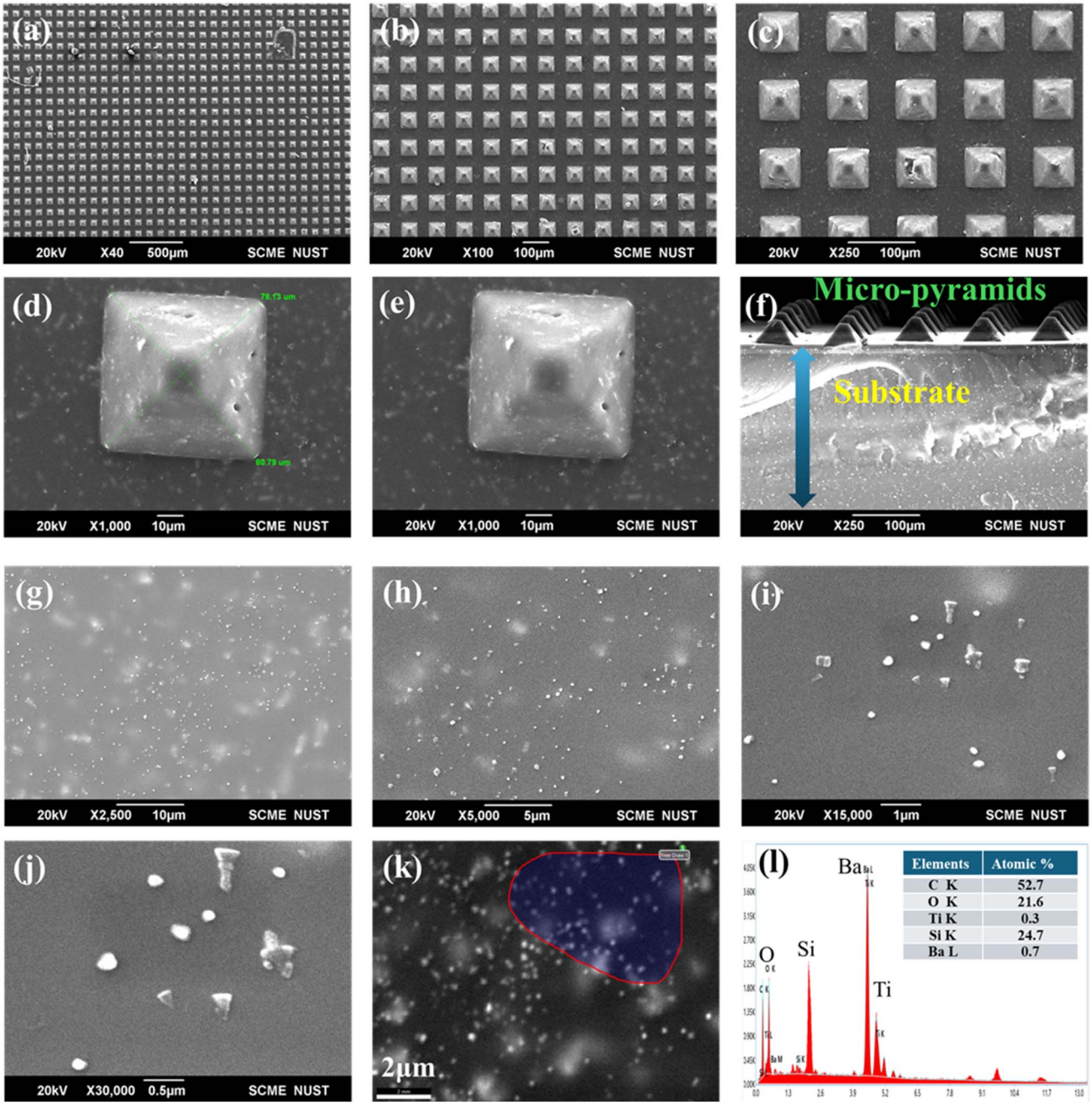

Fig. 6 (a–f) SEM images showing the surface topography of the BT-PDMS composite film with micro-pyramidal structures at various magnifications, illustrating the uniformity and precision of the micro-pyramids. (g–k) SEM images of the pristine BT-PDMS film at different scales, highlighting the distribution of $BaTiO_3$ particles within the PDMS matrix. (l) EDS elemental analysis of the BT-PDMS film, confirming the presence and distribution of elements (Ba, Ti, O, Si, and C) in the composite.

phase (P2), due to the presence of organics and physiosorbed water in the materials, as supported by prior studies.[46–48]

The Raman spectroscopic data for the calcined $BaTiO_3$ (BT) powder is shown in Fig. 7(b), providing comprehensive details on the material's geometry, local symmetry, and crystal structure. Through changes in vibrational modes, Raman spectroscopy, which is renowned for its sensitivity to local crystal structures and symmetry, efficiently records structural changes. A change in the local crystal structure of BT was indicated by an increase in vibrational amplitude.[22] Given that the greater vibrational amplitude indicates a more stable and ordered lattice structure, this shift implies a decrease in lattice disorder. The spectra revealed the tetragonal crystal structure of $BaTiO_3$, characterized as four peaks were observed, each mode corresponding to a particular vibration within the crystal structure. These specific peaks confirm the existence of the tetragonal phase, known as a stable structure for $BaTiO_3$, particularly after calcination. The calcination process appears to have enhanced

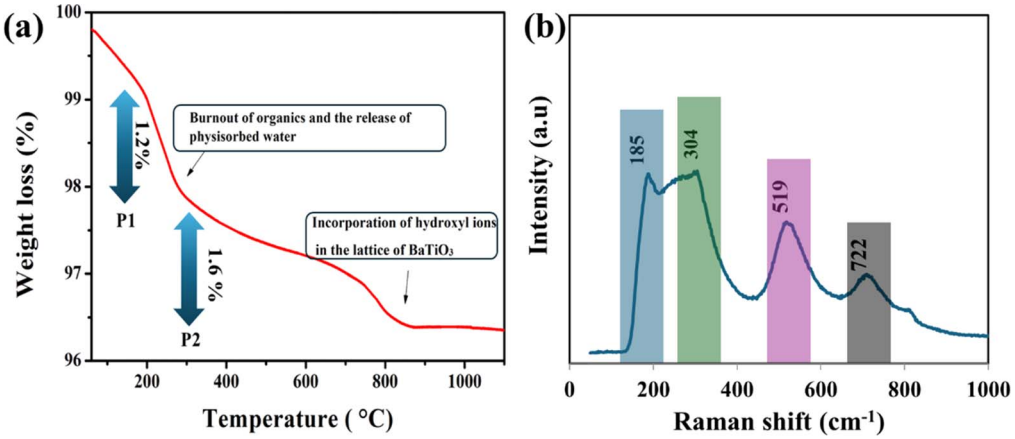

Fig. 7 (a) Thermogravimetric analysis (TGA) of barium titanate powder, showing weight loss as a function of temperature. The two main phases (P1 and P2) indicate the burnout of organics, release of physiosorbed water, and incorporation of hydroxyl ions into the $BaTiO_3$ lattice. (b) Raman spectroscopy of barium titanate powder, displaying characteristic peaks at 185, 304, 519, and 722 cm^{-1}, which correspond to vibrational modes in the $BaTiO_3$ structure.

the material's structural order, as indicated by the increased vibrational amplitudes and the clarity of the peaks. These different modes at 185, 304, 519 and 722 cm^{-1} confirm the presence of the tetragonal phase and unique vibrational in BT powder, which is consistent with previous studies.[23,24] These peaks show the reliability of the calcination process not only stabilized the crystal structure but also reduced the crystal disorder, leading to more distinct vibrational response and enhancement of the material's structural integrity.

Previous work achieved a significant rise in the dielectric constant even below the percolation threshold, in contrast to earlier research that claims an elevation of the dielectric constant near the percolation threshold. The dielectric characteristics of composite systems having a conductive phase scattered throughout an insulating matrix, such as PZT–Ag and PZT–Pt,[62] have been explained by certain research.[59] Such metal–dielectric composites' dielectric response is in good agreement with percolation theory, indicating that the observed rise in the dielectric constant might be attributed to the higher dielectric field created around the metal particles. The electrical and dielectric characteristics of the sintered sample are reported in Table 2.[62]

It is known that using piezoelectric materials in TENG devices could improve their output performance,[3,63,64] Therefore, in our study, a 20% volume fraction of BT was incorporated into PDMS and the resulting composite film was paired with aluminum foil. This choice was made because PDMS and aluminum are positioned far apart in the triboelectric series, suggesting enhanced charge generation. The composite layer acquires a negative charge due to its tendency to gain electrons, while aluminum foil tends to lose electrons, resulting in a positive charge distribution (Fig. 8).

In the initial stage of discussing the piezo response separately in the presence of BT, when the layers have not in contact with each other, the electrical output would be zero as there is no application of pressure now, leaving no net charge on the film surface. When the films come into contact with each other by pressing on the application of force, piezoelectric charges are generated due to the imbalance of electric dipoles caused by the

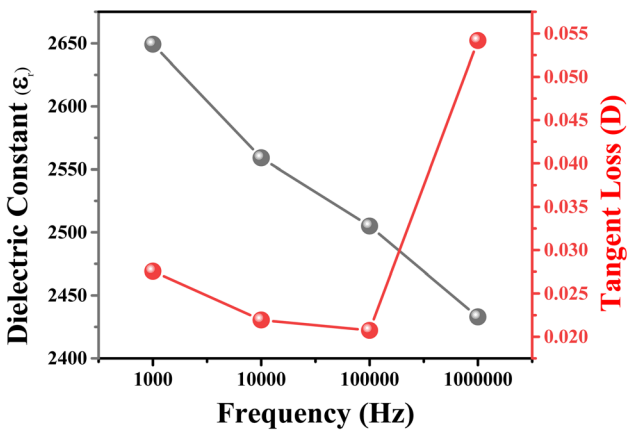

Fig. 8 Dielectric constant (ε) and tangent loss (D) of sintered barium titanate as a function of frequency. The dielectric constant decreases with increasing frequency, while the tangent loss initially decreases before sharply increasing at higher frequencies.

Table 2 Summarize the dielectric and electrical properties of sintered sample

Sr #	Temperature	Sintered density	Dielectric constant (10 kHz)	Tangent loss	Breakdown strength	Figure of merits (10 kHz)
$BaTiO_3$	1150 °C	98%	2560	0.023	1.8	4608

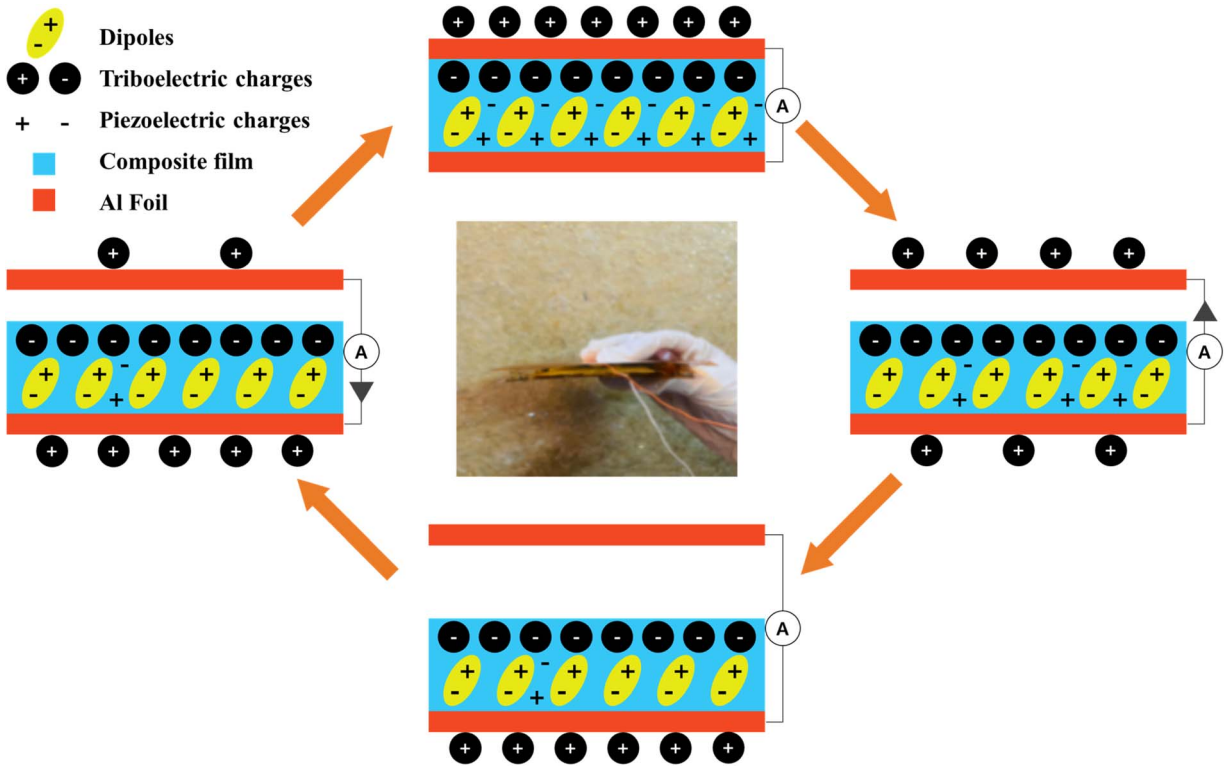

Fig. 9 Schematic illustration of the charge generation mechanism in the HBNG device, highlighting the interaction of dipoles, triboelectric charges, and piezoelectric charges within the composite film and aluminum foil layers. The central image shows the practical application of the device, with arrows indicating the charge flow during mechanical deformation.

stress induced orientation of particles inside the composite film. This leads to the creation of a piezoelectric potential gradient within the film by the appearance of net positive and net negative charges on the opposite surfaces of film, which results in flow of charges and hence the production of current. When the pressing has been done, again there is no flow of

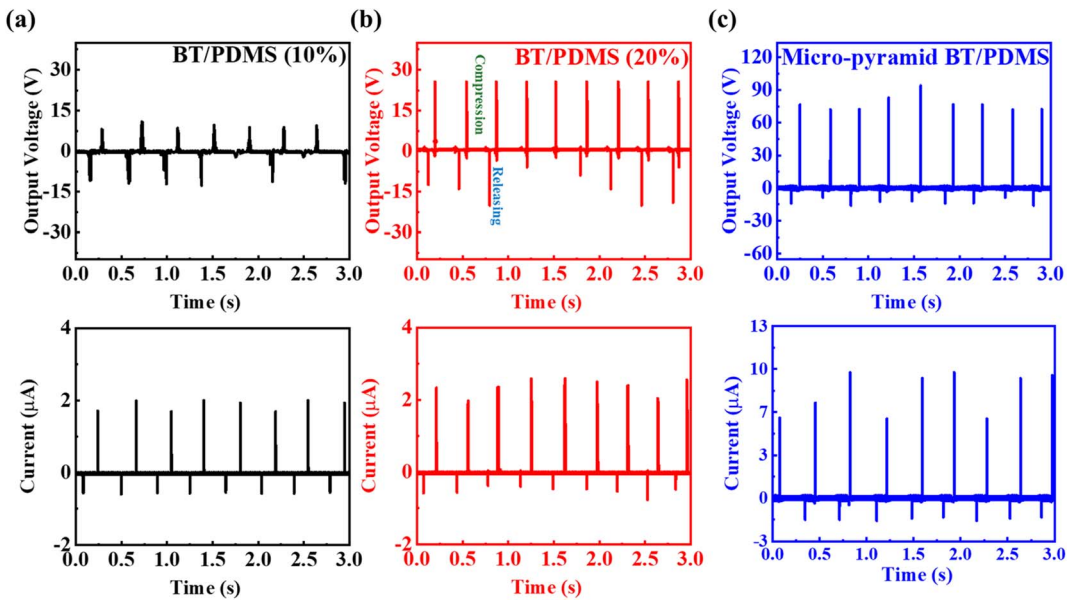

Fig. 10 Output current and voltage of the HBNG device with different surface morphologies: (a and b) standard BT/PDMS composite at 10, 20% concentration, showing moderate voltage and current under compression and release; (c) micro-pyramidal BT/PDMS structure at 20% concentration, exhibiting significantly higher voltage (up to 90 V) and current output due to enhanced surface morphology, demonstrating the performance advantage of the micro-pyramid design.

charges as the deformation of the film has been stopped. As the compressive force is being released, the charges flow back to maintain the equilibrium leading to an output current again and after the compressive force is fully removed, the original state is reached, completing the cycle.

Alongside the piezo response, there is also the generation of triboelectric charges as shown in Fig. 9. The device won't produce any triboelectric charges in the initial state as there is no contact or friction between the triboelectric layers. However, when pressure is applied, the surface of the layers gets in contact with each other, and triboelectric charges are generated. The composite layer would gain electrons from Al foil as it has a stronger affinity for a negative charge, due to this Al foil would attain a positive charge while the composite layer becomes negatively charged. Now the electric polarity has been generated after the pressure is removed and the layers are separated. Due to electrostatic induction, the composite would induce its oppositely generated charges from Al foil to the bottom Al foil, leading to a positive output current when electrons were driven to the top Al foil. The current generated at this point also included the piezoelectric induced charges as mentioned previously, leading to dual phenomenon of triboelectric and piezoelectric effects occurring at the same time which results in enhanced electrical output. When the layers are fully separated by the distance of 1 cm, then there would be no charge transfer due to electrical equilibrium. The pyramid structures strongly influenced the electrical output of the device and there was a huge increase in the values of voltage and current as compared to the device with the regular surface as shown in Fig. 10, due to the increased contact area and there is more charge transfer during friction.

To calculate the output voltage and current of the devices, an oscilloscope was used. To measure the current, a 100 kΩ resistor was used externally to obtain current graphs as shown in Fig. 10. For the HBNG, the contact-separation method was employed to generate the voltage and current, the mechanical force of 800 N was used as the operation condition and both devices had a contact area of 4×4 cm^2 with the test distance between the two layers of about 1 cm. For the contact separation mode, two dissimilar dielectric films are facing each other, and electrodes are attached at the top and bottom of the stacked films, when the films come in contact with each other, it creates oppositely charged surfaces, and a potential drop is created as the films are separated. When the films are connected by a load, free electrons flow in order to balance the electrostatic field, and the potential is dropped again as films come in contact with each other again as shown in Fig. 10.

The oscilloscope readings revealed that the output voltage of the nanogenerator with a regular surface reached at most about 11, 27 V and the output current reached around 2.1, 2.7 μA for

Table 3 Comparison of patterned parameters and their output performance

Samples	Height (μm)	Width (μm)	Distance between patterns (μm)	Pattern density (N cm^{-2})	Output current (μA)	Output voltage (V)
OL-MN	13 118	268	1680	654	109	123
OL-TH-MN	1235	264	13 390	965	117	127
OL-DTH-MN	1528	274	15 787	965	129	167
PD (this work)	34	61	39	10 000	11	92

Table 4 Comparison of recent work done on surface morphology and their output performance

Morphology	Materials	Fabrication method	Operation mode	Output current (μA)	Output voltage (V)	Ref.
Pyramids	ITO/PET-PDMS	Lithography	Linear motor	0.7	18	66
Nano-pattern textile	Ag/PDMS-ZnO	Chemical treatment	Mechanical force simulator	65	120	67
Cubes	ITO/PET-PDMS	Lithography	Linear motor	0.7	18	66
Nano-pillars	Au/PDMS	ICP etcher	130 N, 3 Hz	3.2	83	68
Micro-pillars	Al/PDMS	Lithography	10N, 5 Hz	8.3	72	69
Micro-needle	Al/PDMS	CO_2 laser ablation	Hand tapping	43.1	102.8	70
Overlapped micro-needle	Al/PDMS	CO_2 laser ablation	Hand tapping	109.7	123	65
Overlapped 2-height micro-needle	Al/PDMS	CO_2 laser ablation	Hand tapping	117.6	127	65
Overlapped deep 2-height micro-needle	Al/PDMS	CO_2 laser ablation	Hand tapping	129.3	167	65
Octet truss	$BaTiO_3$	3D printing	Steel ball drop	52	101	22
Microstructured surface	Cu/PTFE	3D printing	Mechanical force simulator	8	3860	71
Curved architect	PTFE/Cu/PP/Cu/PET	3D printing	Mechanical force simulator	0.01	40	72
Micro pyramids	Al/PDMS-BT	Lithography	Hand tapping	140	1300	This work

10 and 20% BT/PDMS, meanwhile for the nanogenerator with pyramid topography, the maximum output voltage reached up to 92 V and the output current reached around 11 μA as shown in Fig. 10(b). From the values, it is evident that the value of voltage increased up to three folds, meanwhile the current increased up to five folds as compared to pristine nanogenerator. In the previous studies, Kai-Hong *et al.* employed three different microneedle patterns on AL/PDMS TENG device, these three patterns included: Overlapped Microneedle (OL-MN), Overlapped Two-Height Microneedle (OL-TH-MN), and Overlapped Deep Two-Height Microneedle (OL-DTH-MN).[65] The density of patterns (D) was such that OL-MN had a pattern density of 654 MN cm^{-2} while OL-TH-MN and OL-DTH-MN had a pattern density of 965 MN cm^{-2}, similarly, the surface contact area of OL-MN, OL-TH-MN, and OL-DTH-MN was 22.91 × 10^3, 24.38 × 10^3, and 29.69 × 10^3 mm^2 and the output current of these devices were 109 μA, 117 μA, and 129 μA as mentioned in Table 3. The parameters of micro-needles and our work are compared, and the results indicated that the output performance of TENG devices is closely related to the pattern density. From the results, it is evident that surface morphology has played a huge role in enhancing the output performance of the device. Some of the recent work done on the surface morphology of TENG devices has been mentioned in Table 4. Researchers have used different methods to employ complex morphology to their material including lithography, chemical treatment, and CO_2 laser ablation as shown and indicated that surface morphology plays a huge role in enhancing the output performance of the TENG devices. The output performance of triboelectric nanogenerators is dependent on the contact surface area of the friction layers and thus for the case of nanogenerator with pyramid topography, the contact area has increased as the surface area would be calculated as "the number of pyramids" multiplied by the "pyramid surface area".[65] The more the number of pyramids, the more would be the effective contact area for enhancing triboelectric properties during contact and separation deformation. The density of patterns (pyramids per cm or PD per cm) is associated with the output performance of the TENG device and is calculated as such:

$$\text{Density } (D) = N/A$$

where as N represents the number of pyramids and A is the total area of the PDMS/BT plane. In our case, the density of patterns is 10 000 cm^{-2} and the area of a single truncated pyramid is 1159 μm^2.

Fig. 11 shows measured output voltages and currents of the energy harvester based on the BT film with 20% concentration

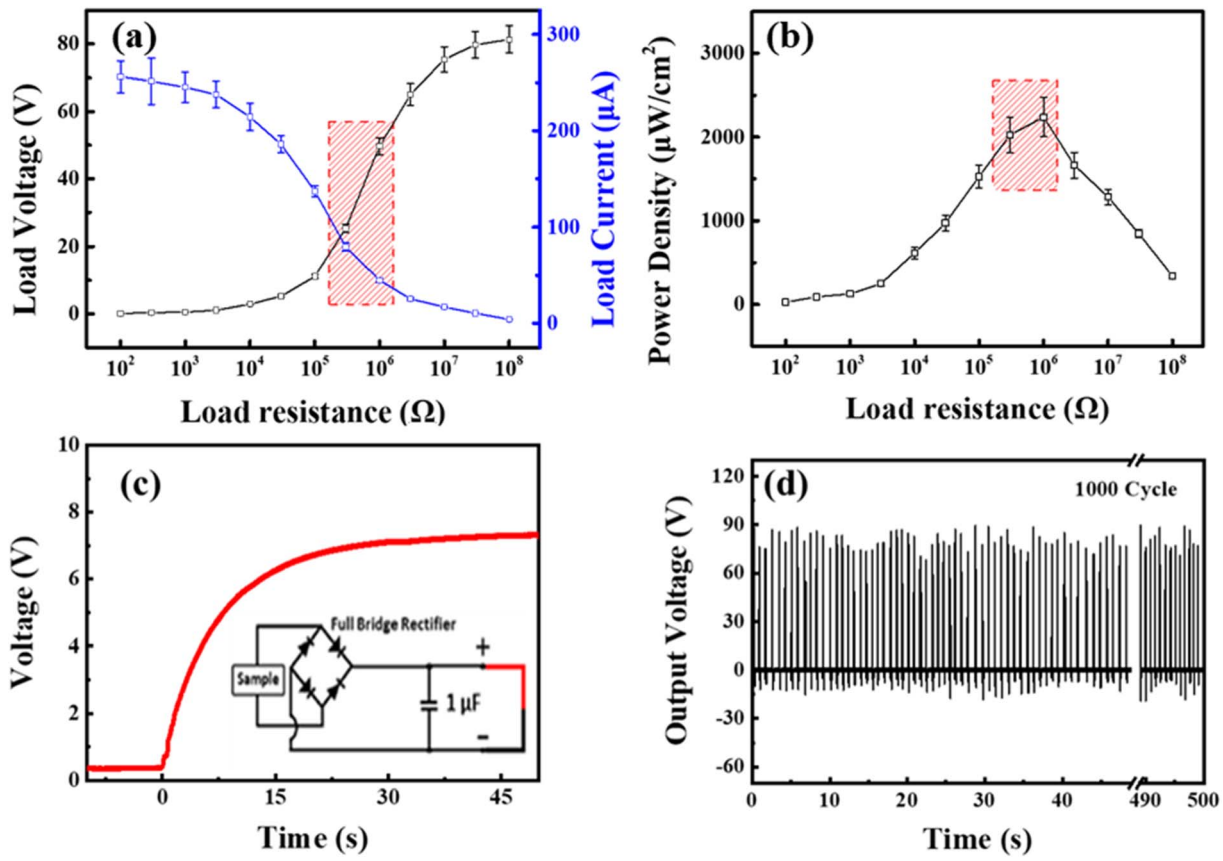

Fig. 11 (a) Open-circuit voltage (black) and short-circuit current (blue) of the micro-pyramidal BT/PDMS HBNG as functions of load resistance, showing the device's electrical response. (b) Power density of the micro-pyramidal BT/PDMS HBNG as a function of load resistance, highlighting optimal power output. (c) Stored voltage in a capacitor circuit using the HBNG, demonstrating energy storage capability. (d) Reliability comparison of the micro-pyramidal HBNG, illustrating performance stability over time.

of PDMS. In HBNG, the performance parameter varies with the load resistance in case of micro-pyramidal BT/PDMS structure. Specifically, V_{oc} and I_{sc} shows the opposite trends according to the load resistance. To measure the generated output power of the energy harvesting system, a load resistor or capacitor was used to measure the maximum output power and energy. The maximum power density was obtained by optimizing the load resistance. As the load resistance increases, the maximum current produced by HBNG decreases. This decline is primarily due to the ohmic losses due to higher resistance, it limits the current flow, leading to the reduction in current output from 250 to 0.2 μA. In contrast, V_{oc} increases as load resistance increases due to the high resistance circuit, the V built across the load. This behavior led to the increase in output load voltage from 76 to 0.5 V.

Fig. 11(b) illustrates the output power generated by the energy harvester, calculated based on the voltage and current across an applied external load. The output voltage and current were calculated by varying the external load resistance, ranging from 100 Ω to 100 MΩ, connected to the BT/PDMS film energy harvester. The output power (P), was determined by:

$$P = I_L V_L$$

where I_L and V_L represent the output current and voltage across the load resistance, respectively. As shown in Fig. 10(b), the output power of the energy harvester first increased and then decreased. The maximum output power was 2500 μW at an optimized load resistance of 37 MΩ, corresponding to a voltage of 23 V and a current of 92 μA. After this peak value, the power generated output decreased. This trend indicates the load resistance at the maximum power transfer occurs for the energy harvester. Additionally, the power density can be expressed as:

$$\text{Power density} = \text{Generated output power/volume}$$

The generated output power of the piezoelectric energy harvester based on the micro-pyramidal BT/PDMS film was 250 mW cm^{-3} based on the device size of 3 × 3 cm^2. Numerous studies have been conducted on HBNG, though most tend to show limitations and low power density. To address this issue, this micro-pyramid BT/PDMS film structural design elevates the frictional contact and surface charge density, resulting in a tremendous increase in power density. Table 4 compares the voltage and current of various TENG, PENG and HBNG, which uses various materials and fabrication techniques under similar pressure conditions. The table shows that our micro-pyramidal BT-PDMS HBNG achieves a significantly higher power density than those in previous studies, demonstrating the effectiveness of this approach in energy output.

The current load (I_L) can be described by the equation:

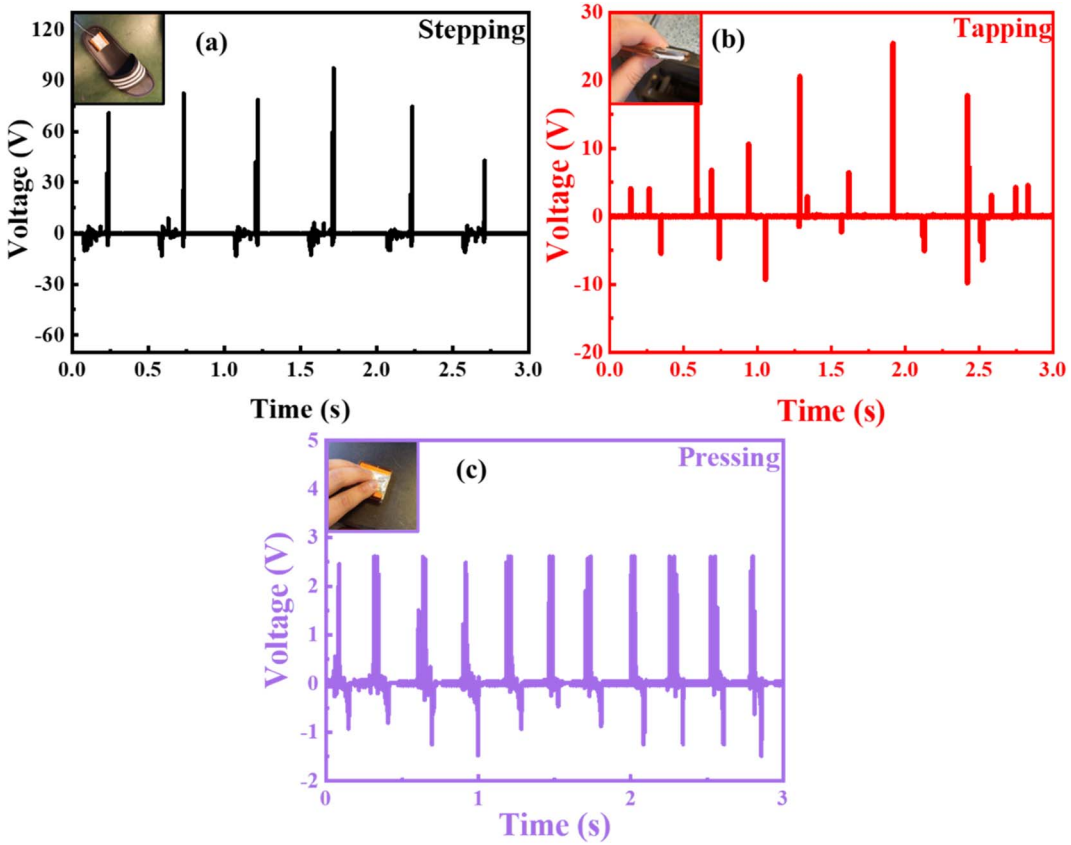

Fig. 12 Output voltage response of the HBNG nanogenerator under different mechanical actions: (a) stepping shows a strong response up to 90 V, ideal for high-impact motion detection; (b) tapping generates peaks up to 30 V, indicating sensitivity to moderate pressure; (c) pressing produces consistent signals around 2.8 V, suitable for low-force sensing applications. Insets depict the testing setup for each action.

$$I_L = V/(R_{HBNG} + R_L),$$

where R_{HBNG} and R_L represent the resistances of the micro-pyramidal BT/PDMS film and the applied external load, respectively. Consequently, the output power across the load P_L can be written as:

$$P_L = I^2 R_L = (V/(R_{HBNG} + R_L))^2 R_L$$
$$= V^2 R_{HBNG}{}^2/R_L + 2R_{HBNG} + R_L$$

The maximum value of P_L occurs at the minimum value of the denominator, and therefore, the derivative of the denominator of R_L can be expressed as:

$$d/dR_L\ (R_{HBNG}{}^2/R_L + 2R_{HBNG} + R_L) = -R^2{}_{HBNG}/R^2{}_L + 1 = 0.$$

Consequently, the maximum P_L value occurs when $R_{HBNG} = R_L$.

In our study, Fig. 11(c and d) show the stored voltage and reliability results of the energy harvester based on the micro-pyramidal BT/PDMS film. Under conventional ceramic capacitors with capacitances of 1 μF, the stored voltage of the energy harvester increased up to 8 V within 50 seconds, when mechanical forces were applied showing the HBNG impressive charging capability. In energy harvesting applications, ensuring electrical output despite the periodic external forces by repeated and intense friction are essential for the performance of the HBNG. A cyclic test, to assess long-term stability, was performed to examine the reliability of the output performance of the film. During this test, HBNG underwent 1000 cycles of pressing and releasing by mechanical forces without any observable drop in the open-circuit voltage (V_{oc}). The maximum value of the voltage is the same at the beginning and the end of the cycle test, showing the stable power generation, the energy harvester showed excellent mechanical resilience and a stable output performance even under constant external pressure. The results demonstrate that the micro-pyramid BT/PDMS film-based energy harvester delivers exceptional output performance with no signs of degradation or fatigue over time.

Fig. 12 presents the output performance and versatile detection capabilities of our HBNG nanogenerator, designed with a micro-pyramidal structure, as depicted in the graphical representation in Fig. 13 under a range of everyday and environmental conditions. The HBNG effectively detected various human and environmental motions, such as pressing, tapping, and stepping, with output signals strengthening as the applied pressure increased (pressing < tapping < stepping). During stepping, the V_{oc} reached a maximum of 92 V, though this output fluctuated due to the irregularity of impact forces. When the device was attached to a human foot, it enabled precise monitoring of real-time activity by capturing subtle V_{oc} pulse patterns, demonstrating its potential for accurate human

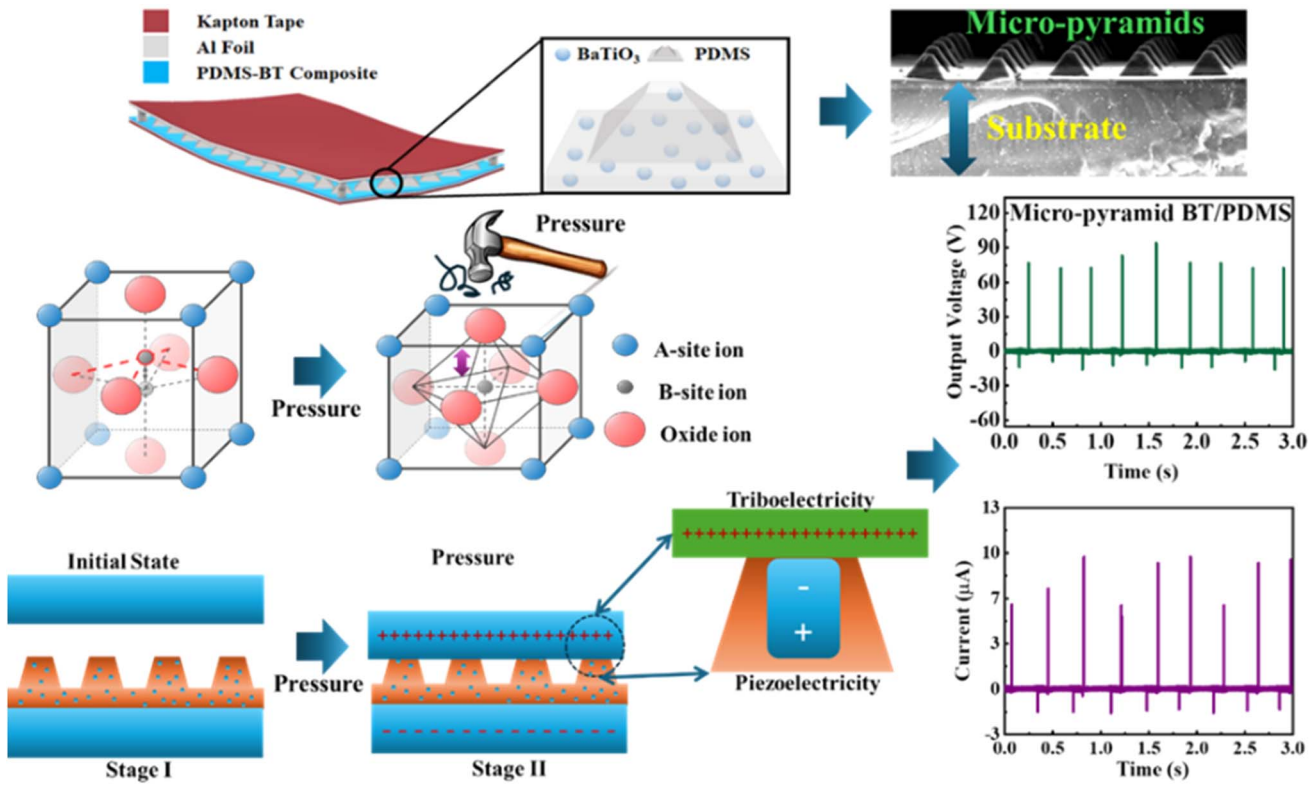

Fig. 13 Schematic illustration of the HBNG nanogenerator with a micro-pyramidal structure, showing the layered composition of Kapton tape, aluminum foil, and PDMS-$BaTiO_3$ composite. The micro-pyramidal substrate design enhances contact sensitivity, facilitating higher output voltages under mechanical stress.

motion tracking. In addition, the device showed robust performance in daily scenarios, generating output voltages of 92 V, 24 V, and 2.8 V under stepping, tapping, and pressing conditions, respectively. These tests were conducted at standard room conditions (23 °C and 47% humidity), underscoring the nanogenerator's adaptability and high sensitivity for a variety of applications, including wearable technology, environmental sensing, and human activity monitoring across different conditions. This performance highlights the HBNG's suitability for flexible, real-world applications.

Conclusion

In summary, a Hybrid Triboelectric and Piezoelectric Nanogenerator was fabricated by using PDMS and barium titanate as the primary materials. The surface morphology of the composite film was changed by employing micro-pyramids to its surface with the help of lithography. For the nanogenerator, PDMS-BT film was used as a tribonegative material, meanwhile, Al foil was used as a tribopositive layer as well as the electrode and contact separation mode was utilized to couple piezoelectric and triboelectric effects together. The pressing of film, induced dipoles in it due to deformation, meanwhile the triboelectric charges were formed due to the contact and separation. The results of output voltage and current indicated that the surface morphology plays a huge role in enhancing the triboelectric effects as increasing the contact surface area can significantly improve its output performance. The density of patterns plays an important role in increasing the friction between the surfaces as well and hence our pattern density (D) of about 10 000 cm^{-2} also contributed largely towards the increments in the values of output voltage and current. These results offer promising strategies for fabricating high-performance and sensitive HBNGs for wearable devices and sensors.

Data availability

The data that support the findings of this study are available from the corresponding authors upon reasonable request.

Author contributions

G. L., F. A., S. U. R., M. Z. K & M. S. conceptualized the study. A. M., M. R. A., U. K., O. S., M. A. M., J. H. K., M. S., G. L. F. A. & M. Z. K characterized and analyze the films. G. L. & M. S. did the writing and characterizations. M. Z. K. & U. K. carried out the measurement. G. L., M. S., O. G., conducted the electrical experiment. U. K., M. Z. K., M. A. M., M. R. A. & A. M. commented on the manuscript. All the authors discussed the results and contributed to the manuscript preparation.

Conflicts of interest

The authors declare no conflict of interest.

Acknowledgements

This work was jointly supported by the National Research Program of Universities (NRPU), the Higher Education Commission, (HEC), Pakistan research fund "Nanogenerators for Self-powered IoT" 20-14492/NRPU/R&D/HEC/2021 and MSIT (Ministry of Science and ICT), Korea, under the ITRC (Information Technology Research Centre) support program (IITP-2025-RS-2020-II201655, 50%) supervised by the IITP (Institute of Information and Communications Technology Planning And Evaluation).

References

1 N. Sezer and M. Koç, A comprehensive review on the state-of-the-art of piezoelectric energy harvesting, *Nano Energy*, 2021, **80**, 105567.
2 H. Liu, *et al.*, A comprehensive review on piezoelectric energy harvesting technology: Materials, mechanisms, and applications, *Appl. Phys. Rev.*, 2018, **5**, 041306.
3 J. Yu, *et al.*, Highly skin-conformal wearable tactile sensor based on piezoelectric-enhanced triboelectric nanogenerator, *Nano Energy*, 2019, **64**, 103923.
4 V. Palaniappan, *et al.*, Laser-Assisted Fabrication of a Highly Sensitive and Flexible Micro Pyramid-Structured Pressure Sensor for E-Skin Applications, *IEEE Sens. J.*, 2020, 1.
5 M. Chorsi, *et al.*, Piezoelectric Biomaterials for Sensors and Actuators, *Adv. Mater.*, 2019, **31**, 1802084.
6 D.-M. Shin, S. W. Hong and Y.-H. Hwang, Recent Advances in Organic Piezoelectric Biomaterials for Energy and Biomedical Applications, *Nanomaterials*, 2020, **10**(1), 123.
7 L. Persano, *et al.*, High performance piezoelectric devices based on aligned arrays of nanofibers of poly(vinylidenefluoride-co-trifluoroethylene), *Nat. Commun.*, 2013, **4**(1), 1633.
8 A. Waseem, *et al.*, Flexible self-powered piezoelectric pressure sensor based on GaN/p-GaN coaxial nanowires, *J. Alloys Compd.*, 2021, **872**, 159661.
9 I. Jeerapan and S. Khumngern, Chapter 9 - Wearable flexible biosensing devices contributing to modern precision medicine, in *Biosensors In Precision Medicine*, ed. L. C. Brazaca and J. R. Sempionatto, Elsevier, 2024, pp. 267–313.
10 B. Arman Kuzubasoglu and S. Kursun Bahadir, Flexible temperature sensors: A review, *Sens. Actuators, A*, 2020, **315**, 112282.
11 S. Qureshi, *et al.*, Review of fabrication of SAW sensors on flexible substrates: Challenges and future, *Results Eng.*, 2024, **22**, 102323.
12 R. Joly, *et al.*, Polymeric cantilevered piezotronic strain microsensors processed by Atomic Layer Deposition, *Sens. Actuators, A*, 2020, **315**, 112280.
13 T. Dinh, *et al.*, Physical Sensors: Thermal Sensors, in *Reference Module In Biomedical Sciences*, Elsevier, 2021.
14 X. Wang, *et al.*, Research progress of flexible wearable pressure sensors, *Sens. Actuators, A*, 2021, **330**, 112838.
15 M. Han, *et al.*, Highly sensitive and flexible wearable pressure sensor with dielectric elastomer and carbon nanotube electrodes, *Sens. Actuators, A*, 2020, **305**, 111941.

16 J.-W. Lee, *et al.*, High sensitivity flexible paper temperature sensor and body-attachable patch for thermometers, *Sens. Actuators, A*, 2020, **313**, 112205.
17 L. Kang, *et al.*, A flexible resistive temperature detector (RTD) based on in-situ growth of patterned Ag film on polyimide without lithography, *Microelectron. Eng.*, 2019, **216**, 111052.
18 A. Waseem, *et al.*, GaN/Al_2O_3 core-shell nanowire based flexible and stable piezoelectric energy harvester, *J. Alloys Compd.*, 2021, **860**, 158545.
19 A. T. Le, M. Ahmadipour and S.-Y. Pung, A review on ZnO-based piezoelectric nanogenerators: Synthesis, characterization techniques, performance enhancement and applications, *J. Alloys Compd.*, 2020, **844**, 156172.
20 R. A. Surmenev, *et al.*, Hybrid lead-free polymer-based nanocomposites with improved piezoelectric response for biomedical energy-harvesting applications: A review, *Nano Energy*, 2019, **62**, 475–506.
21 Ritu, *et al.*, Unveiling a robust and high-temperature-stable two-dimensional ZnAl layered double hydroxide nanosheet based flexible triboelectric nanogenerator, *Nanoscale*, 2024, **16**(8), 4176–4188.
22 J. H. Shi, *et al.*, Ultrahigh Piezoelectricity in Truss-Based Ferroelectric Ceramics Metamaterials, *Adv. Funct. Mater.*, 2024, 2417618.
23 G. Pace, *et al.*, Electrode selection rules for enhancing the performance of triboelectric nanogenerators and the role of few-layers graphene, *Nano Energy*, 2020, **76**, 104989.
24 R. Yue, *et al.*, A review of flexible lead-free piezoelectric energy harvester, *J. Alloys Compd.*, 2022, **918**, 165653.
25 M. Mariello, Recent Advances on hybrid piezo-triboelectric bio-nanogenerators: Materials, architectures and circuitry, *Nanoenergy Advances*, 2022, **2**(1), 64–109.
26 Y. P. Jeon, *et al.*, Enhancement of the output voltage for triboelectric nanogenerators due to Al doping in the zinc oxide layer, *J. Alloys Compd.*, 2020, **831**, 154913.
27 M. T. Chorsi, *et al.*, Piezoelectric biomaterials for sensors and actuators, *Adv. Mater.*, 2019, **31**(1), 1802084.
28 Z. Lin, J. Chen and J. Yang, Recent Progress in Triboelectric Nanogenerators as a Renewable and Sustainable Power Source, *J. Nanomater.*, 2016, **2016**, 5651613.
29 B. Mahapatra, *et al.*, A review on recent advancement in materials for piezoelectric/triboelectric nanogenerators, *Mater. Today: Proc.*, 2021, **46**, 5523–5529.
30 T. Ghomian and S. Mehraeen, Survey of energy scavenging for wearable and implantable devices, *Energy*, 2019, **178**, 33–49.
31 Z. L. Wang, Triboelectric nanogenerators as new energy technology and self-powered sensors – Principles, problems and perspectives, *Faraday Discuss.*, 2014, **176**, 447–458.
32 S. Chatterjee, *et al.*, Recent advancements in solid–liquid triboelectric nanogenerators for energy harvesting and self-powered applications, *Nanoscale*, 2020, **12**(34), 17663–17697.
33 C. Rodrigues, *et al.*, Emerging triboelectric nanogenerators for ocean wave energy harvesting: state of the art and future perspectives, *Energy Environ. Sci.*, 2020, **13**(9), 2657–2683.
34 Y. Liu and C. Hu, Triboelectric nanogenerators based on elastic electrodes, *Nanoscale*, 2020, **12**(39), 20118–20130.
35 H. Chen, *et al.*, Triboelectric nanogenerators for a macro-scale blue energy harvesting and self-powered marine environmental monitoring system, *Sustainable Energy Fuels*, 2020, **4**(3), 1063–1077.
36 X. Zhang, *et al.*, Self-powered triboelectric-mechanoluminescent electronic skin for detecting and differentiating multiple mechanical stimuli, *Nano Energy*, 2022, **96**, 107115.
37 Y. Liu, *et al.*, A one-structure-layer PDMS/Mxenes based stretchable triboelectric nanogenerator for simultaneously harvesting mechanical and light energy, *Nano Energy*, 2021, **86**, 106118.
38 Z. Zhang and J. Cai, High output triboelectric nanogenerator based on PTFE and cotton for energy harvester and human motion sensor, *Curr. Appl. Phys.*, 2021, **22**, 1–5.
39 H. Varghese, *et al.*, A high-performance flexible triboelectric nanogenerator based on cellulose acetate nanofibers and micropatterned PDMS films as mechanical energy harvester and self-powered vibrational sensor, *Nano Energy*, 2022, **98**, 107339.
40 K. V. Vijoy, H. John and K. J. Saji, Self-powered ultra-sensitive millijoule impact sensor using room temperature cured PDMS based triboelectric nanogenerator, *Microelectron. Eng.*, 2022, **251**, 111664.
41 L. K. Anlin, *et al.*, Effects of metal nanoparticles on the performance of PDMS based triboelectric nanogenerators, *Phys. B*, 2022, **639**, 413952.
42 G. Jian, *et al.*, Hybrid PDMS-TiO2-stainless steel textiles for triboelectric nanogenerators, *Chem. Eng. J.*, 2021, **417**, 127974.
43 C. K. Chung and K. H. Ke, High contact surface area enhanced Al/PDMS triboelectric nanogenerator using novel overlapped microneedle arrays and its application to lighting and self-powered devices, *Appl. Surf. Sci.*, 2020, **508**, 145310.
44 S. Sriphan, C. Nawanil and N. Vittayakorn, Influence of dispersed phase morphology on electrical and fatigue properties of BaTiO3/PDMS nanogenerator, *Ceram. Int.*, 2018, **44**, S38–S42.
45 B. Dudem, *et al.*, Nanopillar-array architectured PDMS-based triboelectric nanogenerator integrated with a windmill model for effective wind energy harvesting, *Nano Energy*, 2017, **42**, 269–281.
46 M. Saleem, *et al.*, Polarization and strain behaviors of $0.74BiNaTiO_3$–$0.26SrTiO_3$/$Bi0.5(Na0.8K0.2)0.5TiO_3$ ceramic composite, *Ceram. Int.*, 2016, **42**(12), 13960–13968.
47 M. Saleem, *et al.*, Percolation phenomena of dielectric permittivity of a microwave-sintered $BaTiO_3$–Ag nanocomposite for high energy capacitor, *J. Alloys Compd.*, 2020, **822**, 153525.
48 G. Tanvir, *et al.*, Study of ferroelectric and piezoelectric response of heat-treated surfactant-based $BaTiO_3$ nanopowder for high energy capacitors, *Mater. Sci. Eng. B*, 2023, **287**, 116100.

49 F. Wang and W. Ma, Variation in phase diagrams of strained (011) epitaxial $BaTiO_3$ thin films, *Phys. B*, 2018, **540**, 43–50.
50 A. Madani, *et al.*, Structural and optical properties of Sb–$BaTiO_3$ and Y–$BaTiO_3$ doped ceramics prepared by solid-state reaction, *Opt. Mater.*, 2023, **137**, 113480.
51 H. Dong, *et al.*, Ternary phase diagram and dielectric behavior of $BiFeO_3$–$BaTiO_3$–$SrTiO_3$ solid solutions, *Scr. Mater.*, 2024, **244**, 116028.
52 S. Mahboubizadeh, S. T. Dilamani and S. Baghshahi, Piezoelectricity performance and β-phase analysis of PVDF composite fibers with $BaTiO_3$ and PZT reinforcement, *Heliyon*, 2024, **10**(3), e25021.
53 A. G. Kordlar, J. Koohsorkhi and E. T. Nejad, Barium titanate nanorods on micro-machined silicon substrate for performance enhancement of piezoelectric Nanogenerators (NGs), *Solid-State Electron.*, 2021, **186**, 108168.
54 Y. P. Su, *et al.*, Incorporation of barium titanate nanoparticles in piezoelectric PVDF membrane, *J. Membr. Sci.*, 2021, **640**, 119861.
55 T. Zheng, *et al.*, Piezoelectric calcium/manganese-doped barium titanate nanofibers with improved osteogenic activity, *Ceram. Int.*, 2021, **47**(20), 28778–28789.
56 M. Saleem, Ferroelectric properties and microwave sintering of BaTiO3 synthesized by using the alkoxide-hydroxide sol-gel process, *J. Korean Phys. Soc.*, 2014, **65**, 92–97.
57 X. Wei, *et al.*, 3D printing of piezoelectric barium titanate with high density from milled powders, *J. Eur. Ceram. Soc.*, 2020, **40**(15), 5423–5430.
58 R. De Fazio, *et al.*, New Wearable Technologies and Devices to Efficiently Scavenge Energy from the Human Body: State of the Art and Future Trends, *Energies*, 2022, **15**, 6639.
59 X. Dong, *et al.*, Harvesting Wind Energy Based on Triboelectric Nanogenerators, *Nanoenergy Advances*, 2022, **2**, 245–268.
60 C. Tang, Z. Liu and L. Li, Mechanical Sensors for Cardiovascular Monitoring: From Battery-Powered to Self-Powered, *Biosensors*, 2022, **12**, 651.
61 X. Zeng, *et al.*, Wearable Multi-Functional Sensing Technology for Healthcare Smart Detection, *Micromachines*, 2022, **13**, 254.
62 K. Takagi, *et al.*, Fabrication and evaluation of PZT/Pt piezoelectric composites and functionally graded actuators, *J. Eur. Ceram. Soc.*, 2003, **23**(10), 1577–1583.
63 S. Sriphan, High-Performance Hybridized Composited-Based Piezoelectric and Triboelectric Nanogenerators Based on BaTiO3/PDMS Composite Film Modified with Ti0.8O2 Nanosheets and Silver Nanopowders Co-Fillers, *ACS Appl. Energy Mater.*, 2019, **2**, 3840–3850.
64 M. Zhu, *et al.*, Self-Powered and Self-Functional Cotton Sock Using Piezoelectric and Triboelectric Hybrid Mechanism for Healthcare and Sports Monitoring, *ACS Nano*, 2019, **13**(2), 1940–1952.
65 K.-H. Ke and C.-K. Chung, High-Performance Al/PDMS TENG with Novel Complex Morphology of Two-Height Microneedles Array for High-Sensitivity Force-Sensor and Self-Powered Application, *Small*, 2020, **16**(35), 2001209.
66 F.-R. Fan, *et al.*, Transparent Triboelectric Nanogenerators and Self-Powered Pressure Sensors Based on Micropatterned Plastic Films, *Nano Lett.*, 2012, **12**(6), 3109–3114.
67 W. Seung, *et al.*, Nanopatterned textile-based wearable triboelectric nanogenerator, *ACS Nano*, 2015, **9**(4), 3501–3509.
68 I.-W. Tcho, *et al.*, Surface structural analysis of a friction layer for a triboelectric nanogenerator, *Nano Energy*, 2017, **42**, 34–42.
69 G.-G. Cheng, *et al.*, Effect of argon plasma treatment on the output performance of triboelectric nanogenerator, *Appl. Surf. Sci.*, 2017, **412**, 350–356.
70 V.-L. Trinh and C.-K. Chung, A Facile Method and Novel Mechanism Using Microneedle-Structured PDMS for Triboelectric Generator Applications, *Small*, 2017, **13**(29), 1700373.
71 H. Y. Chen, *et al.*, Multifunctional Triboelectric Metamaterials with Unidirectional Charge Transfer Channels for Linear Mechanical Motion Energy Harvesting, *Adv. Funct. Mater.*, 2024, 2416749.
72 H. Y. Chen, J. H. Shi and A. Akbarzadeh, Curved Architected Triboelectric Metamaterials: Auxeticity-Enabled Enhanced Figure-of-Merit, *Adv. Funct. Mater.*, 2023, **33**(49), 2306022.